Crystalline silicon for photovoltaics

Thomas Kaden[*], Sindy Würzner, Felix Dreckschmidt, and Hans-Joachim Möller

Institute for Experimental Physics, Technical University Bergakademie Freiberg, Leipziger Str. 23, 09599 Freiberg, Germany

[*] Corresponding author: e-mail thomaskaden80@gmx.de, Phone: +49 3731 39 3341, Fax: +49 3731 39 4314

Crystalline silicon is currently the basis of about 95% of all solar cells commercially available. Multicrystalline silicon makes up over the half of this amount. The complex defect occurrence and interaction of defects in this material offers a wide field of research and a high potential for material improvement. Extended lattice defects such as dislocations and grain boundaries are important as recombination and storage centres for metallic impurities. Their control is essential to obtain high efficiencies of the solar cell. Important parameters for the assessment of the final efficiency of the solar cells are the distribution and structure of the defects and their impact on the lifetime of minority charge carriers. The current understanding of the nucleation mechanisms of the most important defects during crystal growth will be described. Interaction processes between mobile impurities and extended defects are important for the recombination activity. Measurements of the recombination behaviour and the contamination level will be presented. Effects on the solar cell efficiency shall be discussed.

1 Introduction In the year 2007, about 95% of all commercial solar cells were made from crystalline silicon, thereof about 50% are multicrystalline silicon (mc-Si) solar cells. The solar conversion efficiencies typically range from 14 to 16% [1, 2]. Laboratory cells exceeding efficiencies of 20% have been demonstrated [3]. The further development is generally driven by cost reduction and efficiency increase as well as an increasing competition with thin film solar cells.

Since about two third of the module cost are silicon material cost, the development of inexpensive silicon feedstock and the efficient use of the material are goals, which are currently pursued [4]. A cheaper production process is offered by the direct purification of metallurgical silicon [5], yielding a feedstock material of lower purity. It has been shown that multicrystalline solar cells with 15% efficiency can be made from such a material. This is a cost advantage over monocrystalline silicon, which requires high purity feedstock [6].

More than 80% of multicrystalline silicon is grown by the Bridgman or related techniques. Ingots with masses of 300-400 kg are produced today and cut into wafers by multi-wire sawing. However, the slicing steps waste about 50% of silicon.

Technologies that reduce the number of slicing steps are continuous ribbon growth techniques. Commercially developed are the Edge-Defined Film-Fed Growth (EFG) - and the String Ribbon (SR) processes, where tubes or sheets are grown. Both production routes yield multicrystalline silicon crystals with different microstructures and impurity levels. This is due to different growth velocity and temperature gradient regimes and the use of different crucible materials.

The performance of multicrystalline solar cells is generally limited by lattice defects, which reduce the minority carrier lifetime. Dislocations, grain boundaries and intragrain defects, such as certain impurities, small clusters of atoms or precipitates, are mainly responsible for the enhanced recombination. Particularly localized regions of high dislocation densities are known to be rather detrimental [7]. Dislocations and grain boundaries are also important because of their gettering and storage capacity for certain mobile, mainly metallic impurities. If dissolved in the lattice most of the metal impurities are very recombination active. Because of the high mobility down to lower temperatures they can accumulate at the core of extended defects, which is energetically more favourable. In the bound state the impurities are in general less recombination active.

The total concentration of many impurities that have been analyzed so far exceeds the concentration of the dissolved species by several orders of magnitudes. Therefore in the as-grown material most of the impurities are bound, mainly at extended defects. These agglomerates of atoms form a reservoir that can release atoms again into the bulk during any thermal steps of the solar cell process. The distribution and concentration in the bulk will depend on the particular thermal process and the binding strength between foreign atom and lattice defect. In most solar cell processes gettering techniques are applied to remove impurities from the photo-active region. This requires that impurities are less tightly bound and released more easily into the bulk at the gettering temperatures. On the other hand, if they could be tightly bound in the inactive state one could reduce the recombination centres in the active volume and also increase the efficiency of solar cells.

In order to obtain a better process control one needs to know more about the state of the foreign atoms and the interaction processes. The problem became more urgent in recent years because silicon feedstock from different production processes and lower purity is used. In particular, directly purified metallurgical silicon, which contains much higher impurity concentrations, may be increasingly used for cost reasons. These higher impurity contents have to be kept in an inactive state or removed in order to improve the material quality. In the following the main factors that determine and limit the efficiency will be described and potential routes for further development shall be discussed.

2 Crystal growth techniques for multicrystalline silicon

2.1 Overview Multicrystalline silicon is either grown by ingot or ribbon techniques [8]. Figure 1 drafts the two different principles. For the sake of completeness it should be mentioned, that mc-Si can also be produced by the well-known Czochralski technique. In order to investigate the influence of crystalline defects on the minority carrier lifetime this technique was recently applied [9].
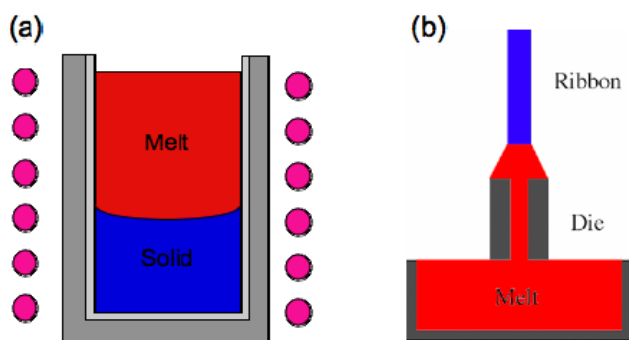

Figure 1 Schematic description of (a) ingot casting/Bridgman technique and (b) edge-defined film-fed growth (EFG) technique.

2.1 Ingot growth In the ingot techniques the crystallization crucibles are either filled with high purity silicon, which is molten inside, or the silicon is molten in a separate crucible and then poured into the crystallization crucible (casting technique). The ingots are crystallized either by the Bridgman or vertical gradient-freeze technique (VGF) and have cross sections today of more than $60 \times 60 \ cm^2$ with a weight over 300-400 kg. The crystallization and cooling processes take about 30 to 40 hours but faster production times will be achieved in the future. The heat extraction must occur in a very controlled manner to maintain a high quality of the crystal. In order to achieve a low dislocation density, the melt interface must be kept planar to ensure low thermal stresses.

Impurities are present in the silicon feedstock in different concentrations depending on the purification processes that has been applied. Additionally, impurities are incorporated through the contact of melt and crystal with the crucible walls and the ambient gas atmosphere. Typical crucible materials are SiO_2 (quartz), Si_3N_4 as a coating layer on the inside and graphite from the support die. Dissolution of these materials introduces the elements oxygen, nitrogen and carbon in various concentrations. In addition, remnant impurities in the crucible materials such as the metals Fe, Cr, Ni or Cu diffuse into melt and solid. The distribution of impurities and doping elements along the growth direction by segregation and the formation of precipitates depend on the growth process and following processing steps. There is also interaction of the various defects, which is complex and certainly not completely understood. In order to improve the crystal quality, there is steady progress in understanding these phenomena.

2.2 Ribbon growth The ribbon or sheet growth techniques require a shaping system to determine the final shape [10]. The sheet growth techniques differ mainly by the shaping system that is used. The ribbon-growth-on-substrate (RGS) - method is distinguished by a crystallization direction perpendicular to the pulling direction [11]. It has the potential of very high production speeds but is still in the development stage. With RGS pull rates of 600 cm/min are obtainable.

The most advanced method is the edge-defined-film-fed-growth (EFG) technique (Fig. 1b). Hereby, crystallization and pulling direction are parallel. In the industrial process a hollow octagon tube is pulled from the melt. The side faces have a width equal to the wafer size and a wall thickness between 200-300 μm. The length of the tube is about 7 m. The tubes are cut into the final wafer size by high-powered lasers. A similar technique is the String Ribbon technique, where several sheets are grown in parallel. The shaping system consists of two thin SiC filaments at the edges of each ribbon.

The growth velocity of the EFG-technique is equal to the crystallization velocity of about 1 cm/min. In order to achieve high production speeds very high temperature gradients of more than 200 K/cm have to be used at the melt

interface. This leads to large thermal stresses in the sheets or tubes and a microstructure consisting of long elongated grain boundaries in growth direction and a high density of dislocations. Another typical feature is the direct contact with the shaping system made from graphite, which introduces a high concentration of carbon into the material. In addition, metal impurities are incorporated from the crucible contact as well.

3 Precipitate formation Oxygen, carbon and nitrogen are the impurities that have to be considered in melt processes. The main sources for the incorporation of these impurities are the silicon feedstock, the crucible walls, the melt feeding parts and the ambient gas phase.

3.1. Formation from the melt For the ingot techniques (Bridgman, VGF) the melt is in contact with the porous coating made of Si_3N_4 and through the pores with the quartz (SiO_2) crucible. The dissolved amount of oxygen and nitrogen depends on the dissolution rate of SiO_2 and Si_3N_4. The structural properties of the coating layer (thickness, porosity etc.) are important here. Furthermore, one has to consider the exchange of gases over the melt surface. Oxygen is lost by evaporation of SiO and carbon is introduced by CO-gas that forms through the oxidation of graphite parts in the crystallization furnace. By controlling the flow of ambient gas (e.g. argon) over the melt surface one can influence the amount of oxygen and carbon in the melt.

The impurities are distributed in the melt by convection and diffusion processes. Because of the different segregation coefficients (oxygen: $k_o = 1.4$, carbon: $k_o = 0.07$, and nitrogen: $k_o = 0.0007$), the impurity distributions that are incorporated in the solid differ considerably. Figure 2 shows experimentally determined distributions of dissolved oxygen (a) and carbon (b) in a crystal grown by the Bridgman technique. Carbon and nitrogen are enriched in the centre of the crystal, whereas the oxygen distribution follows approximately the shape of the melt interface. The patterns can be explained on the basis of the mass distributions in the melt, which can be simulated today quite accurately by simulation programs. A FEM-simulation of a cross section of the crucible for this particular growth process shows two opposite convection rolls with a flow of melt parallel to the melt surface and an upwards stream in the centre (Fig. 2b). Since carbon (and also nitrogen) is less incorporated in the solid, the centre of the melt will be enriched with these impurities as observed. Depending on the growth conditions such as growth velocity and gas flow over the melt surface the enrichment in the melt varies and can even exceed the solubility limit in the melt. The flow pattern of melts in industrial growth furnaces differs from the depicted situation because of other crucible geometries and a larger melt volume.

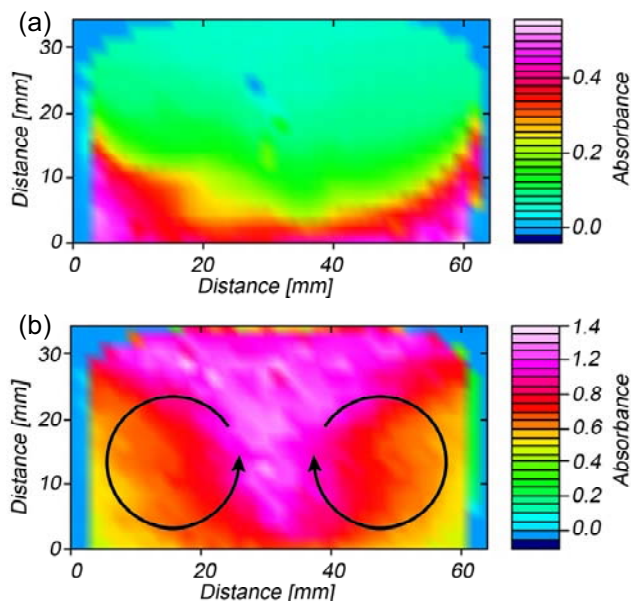The impurity distribution pattern also differs for continuous growth processes. In the EFG ribbon growth the

Figure 2 Topographic FTIR measurement of the distribution of dissolved oxygen (a) and carbon (b) in a vertical cross section of a multicrystalline silicon crystal grown by the Bridgman technique. The corresponding convection flow in the melt is indicated in (b).

melt is continuously replenished with fresh, pure silicon feedstock. Therefore, the average impurity concentrations in the melt are determined by the mixing of high purity silicon with the previously enriched melt.

The main impurity in EFG ribbons is carbon due to the contact of the melt with the graphite parts of the crucible and the shaping system. Most of the carbon is introduced in the crucible part, which is kept at the highest temperature in the system. The melt feeding system supplies the impurity enriched melt to the meniscus region. The distribution of carbon at the solidification front is again determined by diffusion and convection. 2D-FEM simulations of the carbon distribution in the meniscus region show rather high concentrations of about $1 - 2 \times 10^{19}$ cm^{-3}, which is above the solubility limit in the melt.

These and other numerical and experimental investigations of recent years have shown that the concentrations for carbon and nitrogen in the melt may exceed the solubility limit near the melting point both for ingot and ribbon silicon. This can lead to precipitation in the melt. Because of the much higher diffusion coefficient in the melt compared to the solid large precipitates can grow. In fact, large precipitates of Si_3N_4 and SiC have been observed in directionally solidified multicrystalline silicon [12-14]. They mainly occur in form of long filaments, needles or tubes that run in growth direction over several mm, see Fig. 3.

In EFG ribbons the growth of large SiC layers has been observed [15]. The microstructure of EFG ribbons contains regions of a high density of (111) twin boundaries, some of
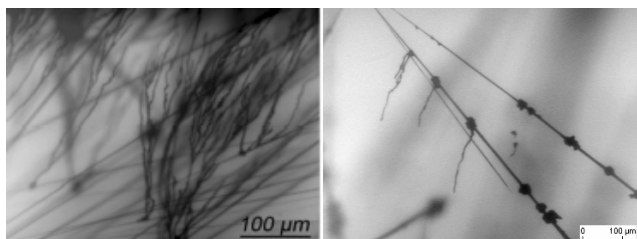
Figure 3 Filaments and precipitates consisting of Si_3N_4 and SiC in multicrystalline silicon.

Figure 4 Schematic phase diagram for carbon and nitrogen.

them are highly stressed. This could be explained by the incorporation of monatomic layers of SiC precipitates [16]. Because of a shorter Si-C bond across the boundary the lattice is contracted here, which causes high local stresses. These layers can extend over several millimetres.

It has been suggested that these precipitates (filaments or layers) form directly at the melt interface [17, 18]. Considering carbon and nitrogen the solidification behaviour can be described schematically for low impurity concentrations by an eutectic two component (A, B) phase diagram with an intermediate phase, here of Si_3N_4 or SiC (see Fig. 4). In both cases there exists a limited solubility in the melt. If the eutectic concentration c_e at the melt interface is exceeded (carbon: $c_e = 4.6 \times 10^{18}$ cm^{-3}, nitrogen: $c_e = 6.4 \times 10^{18}$ cm^{-3}) precipitation may occur. Whether the precipitates nucleate in the melt or at the melt - solid interface depends on the super cooling and the availability of nucleation sites. The most probable process is the heterogeneous nucleation at the melt interface because of the lower interface energy with the solid phase. Nucleation may occur at inhomogeneities, such as grain boundaries or dislocations, that form at the interface during solidification. If solidification takes place at a concentration c_o (of B atoms) above the eutectic concentration c_e the formation of the second phase would occur at a temperature T_1 in thermodynamical equilibrium. However, the formation of the second phase requires nucleation and an undercooling of the melt. The most likely process is heterogeneous nucleation at the melt interface because it requires less undercooling. Therefore, the interface temperature has to be lowered first to the temperature T_o where the liquid begins to solidify and nucleation can occur at the solid - liquid interface.

A precipitate that has nucleated at the interface will grow into the melt with a certain growth velocity v_p, depending on the number of impurity atoms that can be transported to the precipitate by diffusion in the melt. Since the melt interface proceeds at the same time with a velocity v, the final size of the precipitate is determined by the competition of the advancing solidification front and the precipitate growth. If $v > v_p$ the precipitate will be overgrown and incorporated into the solid. If $v < v_p$ the precipitate will grow into the melt and the process will be slowed down or stop because the impurity concentration decreases in front of the melt interface. If $v = v_p$ pre-
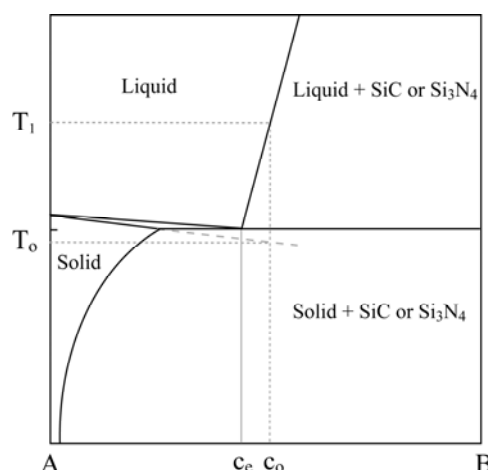
cipitate and interface grow at the same velocity and long precipitates can grow in the direction of crystallisation.

This steady state situation has been analyzed numerically by solving the time independent diffusion equation for different precipitate geometries, namely layers and rods. Numerical estimations show that very long precipitates of several millimetres can occur depending on the supersaturation, the interface velocity and the temperature gradients at the melt interface. Whether rod like or planar structures of the precipitate form depends on the crystallography and interface energies of the phases that form. Obviously planar precipitates are preferred for SiC in twin boundaries and filament structures for Si_3N_4.

For very high supersaturation of carbon and nitrogen in the melt precipitation may even occur in front of the melt interface. Large particles may also break out of the powdery Si_3N_4 coating and be transported directly into the melt without complete dissolution. In both cases the precipitates are finally incorporated by the advancing interface. It has also been suggested that larger particles are pushed by the advancing melt interface before incorporation [19]. This may explain why sometimes very large precipitates or inclusions up to millimetres in size are observed in the solid.

Other impurities such as oxygen or metallic impurities never reach such high concentrations in the silicon melt so that this melt growth mechanism cannot operate. This is in agreement with the observation that the formation of large precipitates ($\gg$ 10 µm) does not occur here. By controlling the oxygen, carbon and nitrogen dissolution from the crucible, the incorporation over the gas atmosphere and the convection in the melt one can suppress the precipitate formation at the melt interface and reduce the amount of impurities that are incorporated in the solid.

3.2 Formation in the crystallized solid The distributions of dissolved oxygen, carbon and nitrogen in the solid show typical features for the different growth pro-

cesses, which correspond to their distribution pattern in the melt as discussed before. In the ingot techniques (Bridgman, VGF) oxygen with a segregation coefficient $k_o > 1$ shows a decrease in the concentration of the dissolved species along the growth direction from the bottom to the top of the solidified crystal. For carbon and nitrogen with $k_o < 1$ the concentration increases. Figure 5 shows typical distributions of the dissolved species measured with Fourier Transformed Infrared (FTIR) spectroscopy.

In growth techniques, where the melt is continuously replenished with fresh, pure silicon the distribution of the elements remains stationary over long periods of time. This is the case for the EFG technique, where the main impurity is carbon. Here, the dissolved carbon distribution in the solid ribbons is characterized by concentration variations of about 40% perpendicular to the growth direction. The origin has not been determined yet but may lie in temperature variations across the side faces of the octagon tube. In general, the carbon concentrations are close to or above the maximum solubility limit at the melting point. The concentrations of oxygen and nitrogen in EFG silicon are much lower compared to ingot silicon (oxygen: $< 1 \times 10^{16} \, \text{cm}^{-3}$, nitrogen: $< 3 \times 10^{15} \, \text{cm}^{-3}$) and are less relevant [20].

The precipitation behaviour of these elements in monocrystalline silicon is well known. An important new aspect in multicrystalline silicon, which has a much higher defect density, is the interaction of impurities with dislocations and grain boundaries. Because of the disturbed crystal structure at the core of the extended defects impurities can accumulate there. Therefore, the total concentration of the elements in the as-grown material consists of the dissolved species and the fraction accumulated at the extended defects during crystal growth.

Transmission Electron Microscopy (TEM) in combination with a chemical (EDX) analyses shows an enrichment of oxygen at dislocations in ingot silicon. The accumulation of oxygen in the strain field of the dislocation is accompanied by the nucleation of small SiO_2 precipitates.

The total oxygen concentration c_{tot} can be determined experimentally by annealing the crystal above the solubility temperature. The gettered oxygen is released then into the bulk and can be determined by FTIR as interstitial oxygen.

Figure 6 shows that in regions of higher dislocation densities more oxygen has been gettered and that c_{tot} decreases with the ingot height in correspondence with the oxygen distribution along the growth direction. The results also show that a large fraction of these elements remains in supersaturation in the as-grown crystals probably because of the limited time for precipitation during the cooling phase of the crystals.

First subsequent annealing for longer periods of time leads to massive precipitation. FTIR investigations of the interstitially dissolved oxygen in ingot silicon show that the concentration decreases considerably in the temperature regime between 700–1100 °C depending on the annealing time. Part of the oxygen accumulates at dislocations then. In addition, bulk precipitates are observed if the starting concentrations are above $3 \times 10^{17} \, \text{cm}^{-3}$. Two types are observed: plate like, crystalline precipitates, which form at temperatures below 800 °C, and spherical amorphous SiO_2 precipitates at higher temperatures. Due to the decreasing oxygen concentration to the top of the ingot bulk precipitation ceases and is not observed anymore.

Precipitation of carbon is in general a very slow process because of the low diffusion coefficient in the solid [21]. At carbon concentrations between 6×10^{16}–$6 \times 10^{17} \, \text{cm}^{-3}$ in ingot silicon the solubility limit is reached between about 1200–1400 °C. At these temperatures the diffusivity is already so slow that most of the carbon remains dissolved after crystal growth. If SiC precipitates occur, they are either small ($< 1 \, \mu m$) or, if larger, have been nucleated in the melt by the mechanisms described above. In EFG ribbons, where the carbon concentration is close or even above the maximum solubility, SiC should precipitate directly after solidification. Due to the fast cooling rate after solidification precipitation is however also suppressed. Recently it has been proposed for EFG ribbons that nanometer size SiC - precipitates still form in the bulk, which may be recombination active [20]. A direct observation was not possible yet, probably because of the very low density.

3.3 Metal impurities Much less is known about the distribution of metal impurities in multicrystalline silicon. Measurements of the total concentration by the Neutron Activation Analyses (NAA) method show large variations for different materials. This is partly due to impurity variations in the feedstock silicon that has been used for the crystal growth. In general, the concentrations are orders of magnitude higher compared to the concentrations of the dissolved species that are determined by electrical measurement techniques. Therefore one must assume that the largest fraction of the impurities are trapped in an electrically inactive or less active form, most likely at extended
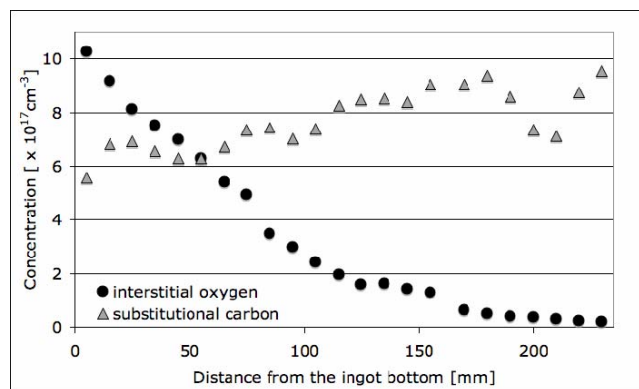

Figure 5 FTIR measurements of interstitial oxygen and substitutional carbon along the growth direction of a mc-Si crystal grown by the ingot technique.
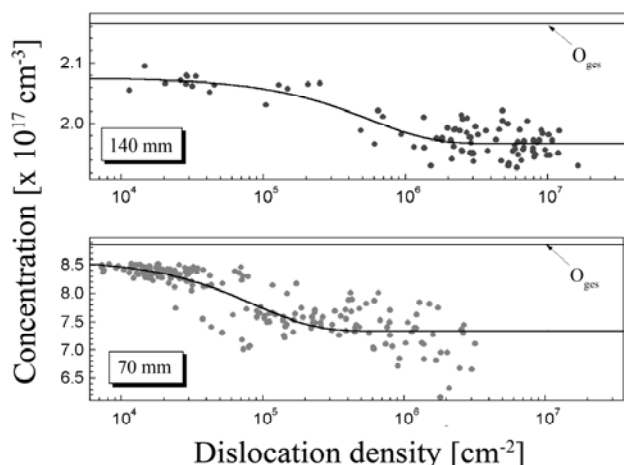
Phys. Status Solidi C **6**, No. 3 (2009)

753

Figure 6 FTIR measurement of the oxygen concentration in dislocated areas as a function of the dislocation density and comparison with the total oxygen concentration. Measurements at two different positions in a mc-Si crystal along the growth direction.

defects such as dislocations, grain boundaries and precipitates of other elements like oxygen, carbon and nitrogen.

The most relevant metal impurities have very low segregation coefficients $k_o \ll 1$. Therefore, one can expect that in ingot growth the concentrations increase in growth direction from the bottom to the top of the solidified crystal. The concentration c_s in the solid can often be described by the Scheil equation, which is valid for complete mixing of the melt and $x < 0.9$

$$c_s = k_{eff}\, c_o\, (1-x)^{k_{eff}-1} \qquad (1)$$

x is the fraction of solidified solid, k_{eff} an effective segregation coefficient and c_o the melt concentration. Particularly for the metals with a high diffusivity deviations of this pattern may occur near the edges of the ingots due to the in-diffusion of further foreign atoms from the contact with crucible walls during the cooling phase. The contaminated regions extend here about 1-2 cm and cannot be used for solar cells with a high efficiency. Since the impurities are also enriched in the top region, where the melt solidifies last, they may diffuse backwards into the bulk if the region stays at elevated temperatures for some time. This back-diffusion has been observed for some metals such as Fe, Co and Cu [22] and can lead to a modified concentration profile.

In general, precipitation of metal impurities during cooling is rarely observed in multicrystalline silicon. Considering that most of the metals are accumulated at dislocations and grain boundaries and very high concentrations may be reached here, one might expect precipitation there. X-ray fluorescence investigations of less pure multicrystalline silicon using synchrotron radiation have shown that nano-scale iron silicate precipitates may occur at grain boundaries [23, 24]. However, very small (nanometre size) precipitates are difficult to detect because of their small size and low density. The experimental results so far indicate that most of the metallic impurities are accumulated at extended defects without precipitation.

4 Dislocation formation during crystal growth
The microstructures of multicrystalline silicon material is considerably depending on the growth technique. In ingot silicon the average dislocation densities vary between 10^4 to 10^6 cm^{-2}. However, bundles of dislocations with densities higher than 10^8 cm^{-2} occur locally and can extend over several centimetres in growth direction. Figure 7 shows such a dislocation distribution in an mc-Si wafer grown by the ingot technique in an area of about 8 cm^2.

In EFG ribbons the microstructure is dominated by heavily twinned regions, where hundreds of (111) twin boundaries extend in growth directions over several centimetres. The width of the twin lamella is in the micrometer range. In the twinned regions the dislocation density is below 10^3 cm^{-2} whereas outside it varies between 10^4 to 10^6 cm^{-2} with high local densities.
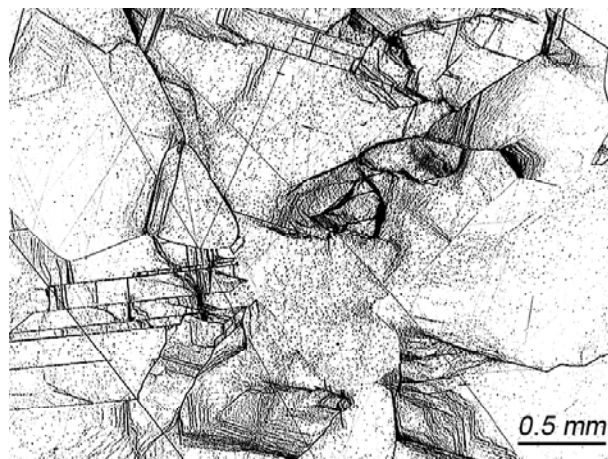

Figure 7 Dislocation distribution in a mc-Si wafer grown by the ingot technique measured by automatic etch pit counting.

Dislocations are formed during crystal growth by plastic deformation while reducing thermal stresses. In EFG ribbons the stress relief occurs partly by twinning, therefore these regions remain mainly dislocation free. The main feature of the dislocated areas is the inhomogeneous distribution of dislocations with high local densities. Some of these dislocation networks show high recombination rates and are thus very detrimental to the lifetime of minority charge carriers. In addition, these dislocations are partly difficult to passivate and thus remain active even in the solar cell.

The origin of the local high densities is not understood yet. It could be shown that dislocation bundles extend over several centimetres in growth direction once they have formed. Since it is difficult to locate the nucleation point of a bundle in a large crystal, not much is known about the stress concentrations that have caused the high local den-

sity. Possible mechanisms are the anisotropic thermal expansion of neighbouring grains or strong lattice distortions around certain types of precipitates.

However, an average dislocation density can be predicted sufficiently well with the model of Alexander and Haasen [25]. This model is based on a physical description of the motion and multiplication of dislocations in the crystal. The basis is the multiplication law for the density N of the mobile dislocations, which is equal to the total density for the early stages of deformation

$$\frac{dN}{dt} = k_1 \, N \, v \, \tau_{eff} \tag{2}$$

whereby k_1 is a proportionality constant, v the dislocation velocity and τ_{eff} the effective stress driving the dislocations. The dislocation velocity depends on the temperature and the stress

$$v = v_0 \, \tau_{eff}^m \, \exp(-U(\tau_{eff})/k_B T) \tag{3}$$

where $U(\tau_{eff})$ is the activation energy of dislocation mobility. The effective stress τ_{eff} is a sum of different contributions:

$$\tau_{eff} = \tau - A \sqrt{N} - G \, \varepsilon_{pl} \tag{4}$$

with

$$A = G \, b \, / \, 2\pi \, (1 - \nu) \tag{5}$$

τ is the external stress acting on the dislocation. In crystal growth it is produced by thermal stresses τ_{th} in the crystal. The second term considers the repulsive interaction with other (mobile and sessile) dislocations, which hinder the motion. G is the shear modulus, b the Burgers vector and ν Poisson's number. In numerical simulations A may also be treated as a free parameter. The third term comes from the stress relaxation through plastic deformation. It is described by the Orowan relation

$$\frac{d\varepsilon_{pl}}{dt} = b \, N \, v \tag{6}$$

The various parameters have been determined experimentally from single crystal deformation experiments for silicon. Figure 8 depicts a numerical solution of the Eqs. (2)–(6) for a constant thermal stress and an exponential time dependence of the temperature (T_m melting temperature)

$$T = T_m \, e^{-t/t_o} \, . \tag{7}$$

An initial density of nucleation sites N_o is assumed here, but the final results are almost independent on the starting value for $N_o < 100$. The results show that there is a steep increase of the dislocation density within the first degrees below the melting point followed by a gradual increase depending on the stress level.

Below about 1000 °C the dislocation density remains almost constant. Depending on the stress level the final dislocation density can vary between 10^4–10^8 cm^{-2}. This is in the regime that is observed experimentally. During the sharp initial increase in the density the dislocations move over large distances of several centimetres. Considering that the grain sizes in a mc-crystal are less then one centimetre, these dislocations will be blocked by grain boundaries. This may be another reason for the observed inhomogeneous distribution of the dislocation density.

There are still uncertainties in the results because some of the used parameters are not known exactly. An important parameter is the activation energy U of the dislocation velocity. Experimental results are only available in the temperature regime up to 1250 °C. It is assumed so far that it has the same value and stress dependence up to the melting temperature.

Realistic simulations have to determine the thermal stresses during crystal growth. The temperature distribution in a furnace and during the growth can be calculate today with sufficient accuracy by FEM simulations [26]. Therefore thermal stresses can be calculated from local temperature differences ΔT according to

$$\tau_{th} = K \, \alpha \, \Delta T \tag{8}$$

where α is the thermal expansion coefficient and K the compression modulus of the solid. In some cases, such calculations have been combined with the model of Alexander and Haasen to determine the evolution of the dislocation density [26, 27]. FEM simulations of large crystals determine the temperature on a length scale of about one centimetre. The crystals are treated as an isotropic solid and the stress components are averaged over a large volume using the von Mises criterion [28, 29]. Therefore, the simulations at present do not allow to simulate the local variations that are observed on the micrometer scale.
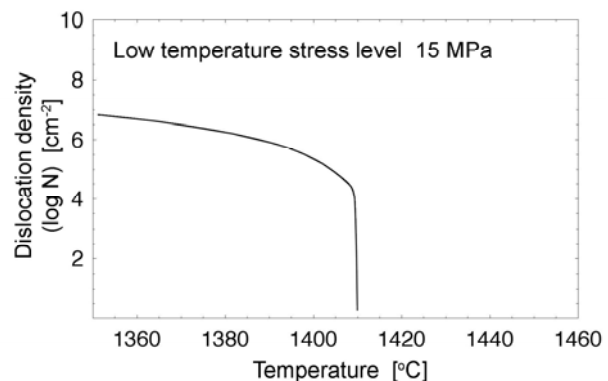
Figure 8 Calculated dislocation density as a function of the decreasing temperature during cooling of a solidified silicon crystal using a low temperature stress level of 15 MPa.

Improvements are possible by taking into account the local polycrystalline structure. Then, stress components on

each (111) glide plane can be determined and the orientation dependence of the dislocation motion taken into account. Local calculations on a finer scale require a multiscaling approach which is much more sophisticated. Such calculations have not been tried yet. It would allow one to determine the influence of parameters such as crystal orientation, change in the dislocation velocity due the interaction with foreign atoms, or variations in the temperature cooling profile during crystal growth. Nonetheless, the present level of simulations gives agreement with experimental results within an order of magnitude and allows to optimize the growth process already to some extent.

5 Recombination behaviour of extended defects In multicrystalline silicon enhanced recombination of minority charge carriers occurs at dislocations, grain boundaries and precipitates. Bulk precipitation only occurs for oxygen, carbon and nitrogen under special growth conditions as described before. Metal precipitation so far has only be observed at dislocations or grain boundaries.

5.1 Precipitates Precipitates of carbon, nitrogen and oxygen are detrimental for solar cells in several ways. Large SiC precipitates (> 10 μm), are hard particles, which could hamper wafer cutting or the fabrication of electrical contacts. SiC and Si_3N_4 precipitates can also be electrically conductive and provide shunting paths through the pn-junction of a solar cell reducing the performance and efficiency. Smaller sub-micrometer precipitates that nucleate in the solid during the cooling phase of crystal growth can also reduce the lifetime.

This is particularly known for oxygen precipitates in monocrystalline silicon, which have been thoroughly studied over decades [30]. The electrical active defects connected with the precipitates are known as New Donors. They are band-like, deep donor states, believed to be related to interface defects between oxide precipitate and silicon lattice. They form in the temperature range between 700–1000 °C. Investigations on multicrystalline silicon show that similar defects also occur here [31]. TEM investigations showed that the previously described plate-like SiO_2 precipitates are responsible for the electrical activity. These defects form after annealing below about 800 °C. Whether they grow already in the as-grown crystals depends on the initial oxygen concentration and the dwelling time during cooling in the critical temperature regime.

The influence of small, sub-micrometer carbon and nitrogen precipitates on the lifetime is less clear because such precipitates have not been observed so far. EFG ribbons have carbon concentrations (up to 9×10^{17} cm^{-3}) higher than the solubility limit and show a reduced lifetime in regions of low dislocation density. Therefore, it has recently been proposed that carbon may form SiC precipitates in the nanometer range, which are recombination active [20]. Carbon and nitrogen can enhance the nucleation of oxygen precipitates, therefore an alternative explanation could be that the observed recombination centres are small induced oxygen precipitates. Since the oxygen and nitrogen concentrations are below the detection limit (O_i: $< 3 \times 10^{15}$ cm^{-3}, N_2: $< 2 \times 10^{14}$ cm^{-3}), the formation of carbon induced oxygen precipitates, which can be observed for higher oxygen concentrations, is unlikely here.

5.2 Dislocations The minority carrier lifetime can be significantly reduced by dislocations especially by regions containing dense dislocation networks. Furthermore, bundles of dislocations are often difficult to passivate in the solar cell process and so reduce the efficiency. Experimental investigations of the recombination activity of individual dislocations have shown that it can change considerably depending on the contamination with impurities [32].

A method for the quantification of the recombination activity of dislocations in solar cells is depicted in Fig. 9 and will be described in the following. A large area is measured topographically by the Light Beam Induced Current (LBIC) technique. Hereby, the solar cell is illuminated locally and the light-induced current is measured. Simultaneously, the reflected light can be detected, which allows one to convert the LBIC signal into the local internal quantum efficiency (IQE). After removing the structure of the solar cell by etching and polishing, the dislocation density is determined by etch pit counting in the same area. The IQE values and the dislocation density are locally correlated. In the case that the recombination properties of the dislocations in the investigated region are equal, one obtains diagrams as shown in Fig. 10. Typically, the IQE is reduced at higher dislocation densities above 10^5 cm^{-2}.

The IQE values can be converted into the local diffusion length L_D of minority carriers using a solar cell simulation program, e.g. PC1D. The diffusion length data can be fitted very well to a theoretical model developed by Donolato [33]. In combination with the PC1D program one can also fit IQE values directly to the dislocation density data [34]. Two parameters are obtained: the bulk diffusion length L_0 (without dislocations) and the normalized recombination strength of the dislocations $\Gamma = V_D/D$. V_D is the dislocation recombination velocity and D the diffusion coefficient of the minority carriers. Whereas the bulk diffusion length is constant over large areas of a solar cell, Γ
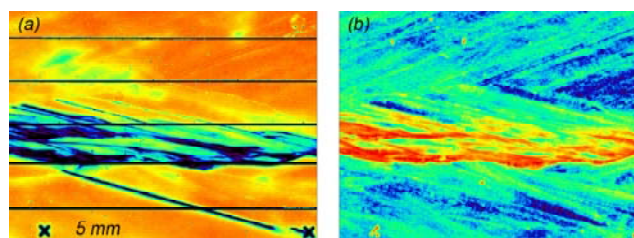

Figure 9 Map of IQE measured by LBIC (a) and dislocation density map (b) in the same area of a mc-Si solar cell.
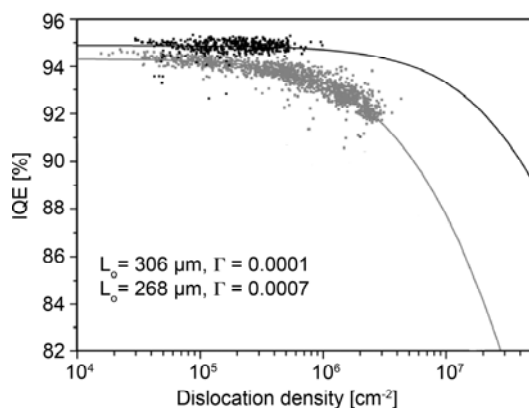
Figure 10 Local correlation of IQE values with the dislocation density in a mc-Si solar cell. Fitted curves from the Donolato-Rinio model yield bulk lifetime L_o and average recombination strength Γ of the dislocations.

varies typically between $\Gamma = 0.0001–0.001$. These variations are explained by different degrees of contamination with mainly metallic impurities.

The same technique can also be applied to wafers before solar cell processing by a direct measurement of the diffusion lengths with the Surface Photovoltage (SPV) method.

6.3 Grain boundaries A further method the to investigate the recombination in solar cells is the electroluminescence (EL) technique. Hereby, the infrared light emission from a solar cell under forward bias is measured spatially resolved with an InGaAs-camera at room temperature [35]. Combining the camera with an IR-spectrometer, spatial resolved EL measurements can be combined with spectral resolved measurements in the wavelength range from 980–1700 nm. EL images recorded with the InGaAs CCD camera contain contributions of the band-to-band recombination with a centre wavelength of 1150 nm and of the defect emission at longer wavelengths. Using appropriate filters, one can exclude a certain wavelength range, e.g. below 1500 nm. Figure 11 shows an EL image using such a filter. Here, only the emission of the so-called defect band is detected.

Certain crystal defects show an enhanced emission. Spatially high resolved measurements and comparison with microscope images of the sample indicated that the defect band emission mainly arises from grain boundaries. Depending on the decoration with impurities only particular grain boundaries show such an emission. As demonstrated in Fig. 12, not each recombination active grain boundary (IQE map in the upper right corner) is responsible for defect band emission. The comparison with the dislocation density map (lower right image in Fig. 12) demonstrates, that dislocations are not responsible for the defect band emission or at least only with intensities below the detection limit of the CCD camera.
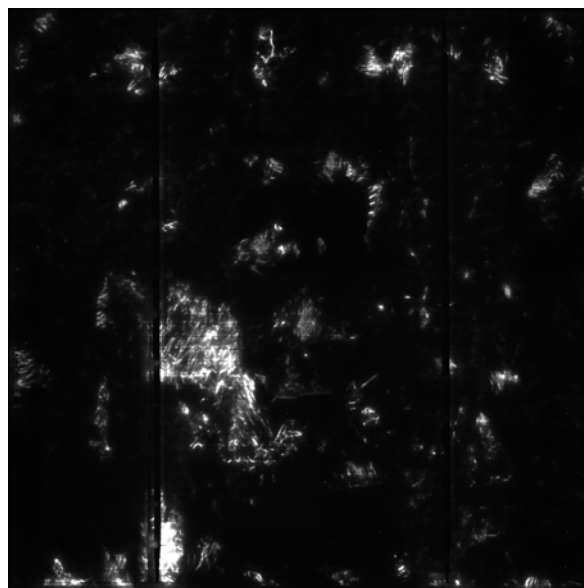

Figure 11 Spatial resolved defect band emission of a mc-Si solar cell in the wavelength range of 1500–1700 nm. Bright regions denote strong luminescence.
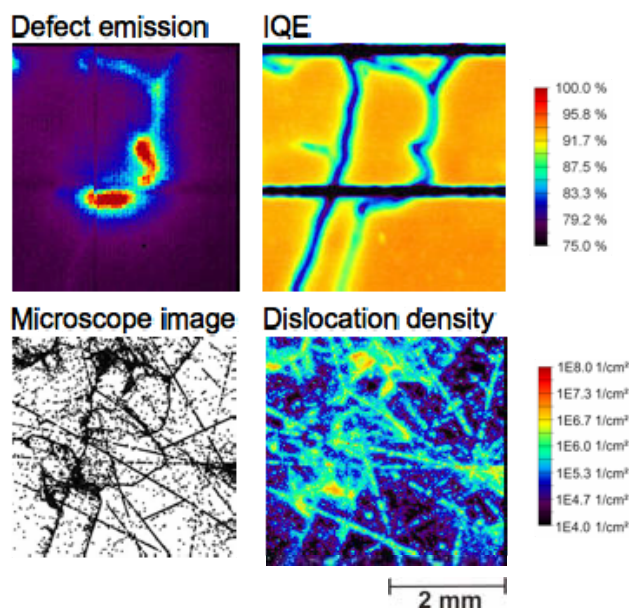

Figure 12 Map of IQE measured by LBIC (a) and dislocation density map (b) in the same area of a mc-Si solar cell.

7 Summary The presented results show that extended defects in multicrystalline silicon come into existence in different temperature regimes during crystal growth. Large precipitates of oxygen, carbon and nitrogen can nucleate first at the melt interface. This process depends on the impurity level in the melt and at the solidification front. It can be suppressed by controlling the interaction with the crucible, the gas flow over and the convection in the melt.

Dislocations form immediately after solidification and their density increases down to temperatures of about

Phys. Status Solidi C **6**, No. 3 (2009)

757

1000 °C. Keeping the thermal stresses low during cooling, one can reduce the dislocations density to levels below 10^5 cm^{-2}. It is not clear yet how to avoid the observed local regions of high density. In combination with improved numerical simulations of the dislocation density one may be able to identify temperature regimes which are particular harmful. A further possibility is to modify the dislocation velocity by solid solution hardening, e.g. with germanium as an isoelectronic element in silicon, causing a strong lattice distortion.

When the solubility limit of impurities is exceeded precipitation may occur. Oxygen and carbon are the impurities with the highest concentrations. Carbon precipitation is so slow that it may only occur at very high impurity concentrations such as in EFG ribbon silicon. Whether SiC precipitates of nanometer size occur could not been confirmed yet. Oxygen at the concentrations levels observed for mc-ingot silicon begins to precipitate below about 1100 °C. Since the precipitates are rather detrimental, this process has to be avoided either by reducing the oxygen level or by reducing the time for growth.

Metallic impurities occur in very high concentrations so far. They are mostly trapped at dislocations and grain boundaries but are released into the bulk during solar cell processing. Gettering takes place at temperatures below 600 °C depending on the impurity. The contamination of dislocations (and grain boundaries) increases their recombination activity. On the other hand, the metal impurities are removed from the bulk, where they are even more detrimental. A better understanding of the interaction and storage processes is required to improve the material in a controlled way.

References

[1] H. Lautenschläger, F. Lutz, C. Schetter, U. Schubert, and R. Schindler, Proc. 14th Europea. PVSEC, Bedford UK, p. 1358 (1997).

[2] J. M. Gee, R. R. King, and K. W. Mitchell, in Proc. IEEE 25th Photovolt. Specialist Conference (P. Basore, IEEE, New York, 1996), p. 409.

[3] O. Schulz, S. Glunz, and G. P. Willeke, Progr. Photovoltaics: Research and Applications **12**, 553-558 (2004).

[4] A. Müller, M. Ghosh, R. Sonnenschein, and P. Woditsch, Mater. Sci. Eng. B **134**, 257 (2006).

[5] H. A. Aulich, F.-W. Schulze, and J. Grabmeier, Chem. Ing. Techn. **56**, 667 (1984).

[6] H. de Moor and A. Jäger-Waldau, in: Proc. PVNET Workshop Proceedings "RTD Strategy for PV"; Special Publication: S.P.I.02.117 (European Commission, DG Joint Res. Centre, Ispra, 2002).

[7] M. Rinio, S. Peters, M. Werner, A. Lawerenz, and H. J. Möller, Solid State Phenomena **82-87**, 701 (2002).

[8] H. J. Möller, Handbook of Semiconductor Technology– Electronic Structure and Properties of Semiconductors, Vol. 1, K. A. Jackson and W. Schröter (Eds.) (Wiley-VCH, Weinheim, 2000), p. 715.

[9] T. Taishi, T. Hoshikawa, M. Yamatini, K. Shirasawa, X. Huang, S. Uda, and K. Hoshikawa, J. Cryst. Growth **306**, 452 (2007).

[10] F. W. Wald, J. Cryst. Growth **87**, 232 (1987).

[11] H. Lange and I. Schwirtlich, J. Cryst. Growth **104**, 108 (1990).

[12] A. K. Soiland, E. J. Ovrelid, T. A. Engh, O. Lohne, J. K. Tuset, and O. Gjerstad, Mater. Sci. Semicond. Process. **7**, 39 (2004).

[13] A. Lawerenz, M. Ghosh, K. Kremmer, V. Klemm, A. Müller, and H. J. Möller, Solid State Phenomena **95/96**, 501 (2004).

[14] C. Reimann, J. Friedrich, G. Müller, S. Würzner, and H. J. Möller, Proc. 21th European PVSEC, Milan, 1073 (2007).

[15] S. Rajendran, M. Larrousse, B. R. Bathey, and J. P. Kalejs, J. Cryst. Growth **128**, 338 (1993).

[16] H. J. Möller, Solid State Phenomena **95/96**, 181 (2004).

[17] J. P. Kalejs and B. Chalmers, J. Cryst. Growth **79**, 487 (1986).

[18] H. J. Möller, Kinetics of Phase Transformations, MRS Symposia Proc. **205**, 476 (1991).

[19] K. A. Jackson and J. D. Hunt, Trans. Metall. Soc. AIME **236**, 1129 (1966).

[20] S. Scholz, Dissertation, TU Bergakademie Freiberg (2008).

[21] R. Newman and J. Wakefield, J. Phys. Chem. Solids **19**, 230 (1961).

[22] D. Macdonald, A. Cuevas, A. Kinomura, Y. Nakano, and L. Geerligs, J. Appl. Phys. **97**, 033523-1 (2005).

[23] A. A. Istratov, W. Huber, and E. R. Weber, Appl. Phys. Lett. **85**, 4472 (2004).

[24] S. McHugo, A. Thompson, A. Mohammed, G. Lamble, I. Perichaud, S. Martinuzzi, M. Werner, M. Rinio, W. Koch, H. Höfs, and C. Hässler, J. Appl. Phys. **89/8**, 4282 (2001).

[25] H. Alexander and P. Haasen, Solid State Phys. **22**, 27 (1968).

[26] D. Franke, Dissertation, RWTH Aachen (2000).

[27] N. Banos, J. Friedrich, and G. Müller, J. Cryst. Growth (2008), in press.

[28] C. T. Tsai, M. W. Yao, and A. Chait, J. Cryst. Growth **125**, 69 (1992).

[29] X. A. Zhu and C. T. Tsai, J. Appl. Phys. **97**, 43520 (2005).

[30] Oxygen, Carbon, Hydrogen and Nitrogen in Crystalline Silicon, Mater. Res. Soc. Symp. Proc. **59** (1986).

[31] D. Yang and H. J. Möller, Solid State Phenomena **82-84**, 707 (2002).

[32] S. Scholz, F. Dreckschmidt, T. Kaden, H. J. Möller, and A. Seidl, Proc. 21st European PVSEC, Dresden, 354 (2006).

[33] C. Donolato, J. Appl. Phys. **84**, 2656 (1998).

[34] M. Rinio, S. Peters, M. Werner, A. Lawerenz, and H. J. Möller, Solid State Phenomena **82-84**, 701 (2002).

[35] F. Dreckschmidt, T. Kaden, H. Fiedler, H. J. Möller, Proc. 22nd European PVSEC, Milan (2007).